Impact of Phantom Size on Low-Energy Virtual Monoenergetic Images of Three Dual-Energy CT Platforms

Joël Greffier *, Claire Van Ngoc Ty, Isabelle Fitton, Julien Frandon, Jean-Paul Beregi, Djamel Dabli

Posted Date: 8 August 2023

doi: 10.20944/preprints202308.0549.v1

Keywords: Dual-energy; Multidetector Computed tomography; Task-based image quality assessment; Split-filter

Article

Impact of Phantom Size on Low-Energy Virtual Monoenergetic Images of Three Dual-Energy CT Platforms

Joël Greffier [1,*], Claire Van Ngoc Ty [2], Isabelle Fitton [2], Julien Frandon [1], Jean Paul Beregi [1] and Djamel Dabli [1]

[1] IMAGINE UR UM 103, Montpellier University, Department of Medical Imaging, Nîmes University Hospital, Nîmes, France
[2] Université de Paris; Assistance Publique Hôpitaux de Paris, Hôpital Européen Georges Pompidou, Department of Radiology
* Correspondence: joel.greffier@chu-nimes.fr; Tel.: +33.04.66.68.33.10

Abstract: To compare the quality of low-energy VMIs obtained with three DECT platforms according to phantom diameter. Three sections of the Mercury Phantom 4.0 were scanned on two generations of split-filter CTs (SFCT-1st and SFCT-2nd) and on one Dual-source CT (DSCT). Noise power spectrum (NPS), task-based transfer function (TTF) and detectability index (d') were assessed on VMIs from 40 to 70keV. Highest noise magnitude values were found with SFCT-1st and noise magnitude was higher with DSCT than with SFCT-2nd for 26-cm (10.2±1.3%) and 31-cm (7.0±2.5%), and the opposite for 36-cm (-4.2±2.5%). The highest average NPS spatial frequencies and TTF values at 50% (f_{50}) values were found with DSCT. For all energy levels, f_{50} values were higher with SFCT-2nd than SFCT-1st for 26-cm (3.2±0.4%) and the opposite for 31-cm (-6.9±0.5%) and 36-cm (-5.6±0.7%). The lowest d' values were found with SFCT-1st. For all energy levels, d' values were lower with SFCT-2nd than with DSCT for 26-cm (-6.2±0.7%), similar for 31-cm (-0.3±1.9%) and higher for 36-cm (5.4±2.7%). In conclusion, compared to SFCT-1st, SFCT-2nd exhibited lower noise magnitude and higher detectability values. Compared with DSCT, SFCT-2nd had lower noise magnitude and higher detectability for the 26-cm but the opposite was true for the 36-cm.

Keywords: dual-energy; multidetector computed tomography; task-based image quality assessment; split-filter

1. Introduction

In recent years, numerous technological developments and innovations have emerged in CT imaging, leading to better radiological management of patients [1–11]. Among them, dual-energy spectral imaging has emerged to improve the detection and characterization of lesions, particularly abdominal lesions [12–15]. Its basic principle is to acquire or detect two photon spectra at low- and high-energy levels to help identify tissue attenuation coefficients. To achieve this, various dual-energy CT (DECT) platforms have been developed [1,2,16–18].

Among the various DECT platforms, one manufacturer has developed two platforms for obtaining two-photon spectra during acquisitions: the dual-source CT (DSCT) platform and the split filter CT (SFCT) platform [1,16]. For the DSCT platform, two X-ray tube/detector pairs (95° offset for 3rd generation) are used to acquire image datasets. The X-ray tube "A" uses low kVp (70, 80, 90, 100 kVp) and the other X-ray tube "B" uses high kVp with (Sn150 kVp) or without a tin filter (140 kVp). With this platform, spectral acquisitions can be made with 5 pairs of kVps and the choice of these pairs depends on the clinical indication for the CT examination and the patient's morphology. For the SFCT platform, the photon beam is split into two-energy spectra using two filters placed at the outlet of the X-ray tube used. The gold filter (Au) is used for the low-energy spectrum and the tin filter (Sn) for the high-energy spectrum. In the first-generation platform (SFCT-1st), the gold filter is

 doi:10.20944/preprints202308.0549.v1

0.05 mm thick and the tin filter, 0.6 mm. In the second-generation platform (SFCT-2nd) the thickness of the gold filter has been increased to 0.07 mm and, conversely, the thickness of the tin filter has been reduced to 0.40 mm. For the SFCT-1st, only 120 kVp can be used to acquire spectral image datasets whereas 120 and 140 kVp can be used for the SFCT-2nd.

Numerous studies have highlighted differences in spectral performance between SFCT-1st and DSCT [16,17]. Using two X-ray tubes provides good spectral separation for DSCT. Otherwise, with SFCT, spectral separation is more limited, due to the overlap between the low- and high-energy spectra generated by the two filters. These differences in spectral performance translate into increased image noise and poorer lesion detectability on the virtual monoenergetic images (VMIs) at low energy levels [16,17]. However, to the best of our knowledge, no studies have ever evaluated the impact of modifying the thickness of the two filters on the spectral performance of SFCT-2nd, especially compared with SFCT-1st and DSCT. In addition, spectral image quality is also influenced by patient morphology and the associated dose level. Euler *et al.* evaluated the impact of phantom diameter and dose level on the spectral performance of the DSCT platform [19]. However, no similar studies have been conducted on the two generations of SFCT platforms.

The purpose of our study was to compare the spectral performances of three DECT platforms according to phantom diameter. Spectral performances were assessed by carrying out a task-based image quality assessment on VMIs.

2. Materials and Methods

2.1. Phantom

The three largest sections (26, 31, 36 cm-diameter) of the Mercury v4.0 phantom (Gammex) were used to perform the task-based image quality assessment (Figure 1A). These three sections have diameters corresponding to the abdomen of patients with a body mass index of 18, 27 and 36 kg/m², respectively [20]. Each section of the phantom is made up of a homogeneous zone with which the Noise Power Spectrum can be calculated (NPS; Figure 1B) and a section with 5 inserts for calculating the Task-based Transfer Function (TTF), particularly on the iodine insert at 10 mg/ml (Figure 1C).

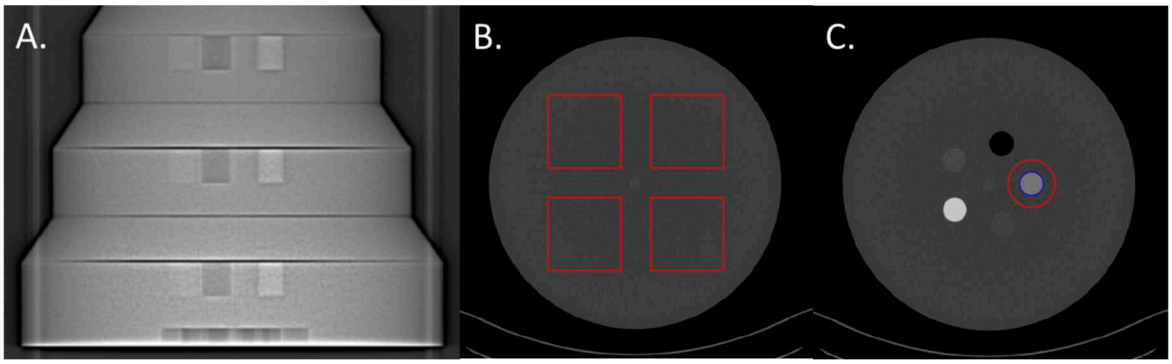

Figure 1. A. Front X-ray image of the 26, 31 and 36 cm-diameter sections of the Mercury v4.0 phantom. **B.** Example of the four regions of interest (ROIs) placed in the homogenous part of the 31cm-diameter section and used on VMIs to assess the noise power spectrum (NPS). **C.** Example of the ROI placed around the iodine insert of 10 mg/ml and used to compute the task-based transfer function (TTF).

2.2. CT scanners and scanning protocol

Acquisitions were performed on three Siemens Healthineers DECT systems, the SOMATOM Force (DSCT) and two generations of SFCT: the SOMATOM Edge (SFCT-1st) and the SOMATOM X.Cite (SFCT-2nd).

For each CT system, the acquisition and reconstruction parameters usually used in clinical practice for abdomen DECT examination were selected (Table 1). For each CT system, the automatic tube current system was disabled and tube currents were set to obtain a volume CT dose index (CTDIvol) of 12.0, 9.1 and 6.9 mGy for the 36 cm, 31 cm and 26 cm-diameter phantoms, respectively.

Preprints (www.preprints.org) | NOT PEER-REVIEWED | Posted: 8 August 2023 doi:10.20944/preprints202308.0549.v1

These dose levels correspond to those usually used on these 3 CT systems for DECT abdomen-pelvis examinations, according to the patient's morphology. Each acquisition was repeated 10 times.

Table 1. Acquisition parameters used for the three CT systems.

CT scan model		SOMATOM Edge	SOMATOM X.Cite	SOMATOM Force
SFCT system generation		1st generation	2nd generation	-
AuSn filter thickness	Au (mm)	0.05	0.07	-
	Sn (mm)	0.60	0.40	-
Tube voltage (kVp)		AuSn120	AuSn120	100/Sn150
Pitch factor		0.3	0.3	0.6
Rotation time (rot/s)		0.33	0.3	0.5
Beam collimation (mm)		38.4	38.4	38.4
$CTDI_{vol}$ (mGy)	26 cm-diameter	6.89	6.95	6.86
	31 cm-diameter	9.10	9.18	9.10
	36 cm-diameter	11.99	12.15	12.04

Raw data were reconstructed using Level 3 of the iterative reconstruction algorithm ADMIRE (ADvanced Modeled Iterative REconstruction) on each CT system. For all systems, the quantitative reconstruction kernel (Qr40), a slice thickness of 1 mm and a 380 mm field of view were used. For each acquisition, VMIs for the 4 lowest energy levels (40/50/60/70 keV) were reconstructed on Syngo.via software (VB60A_HF03) with the specific Monoenergetic Plus application.

2.3. Task-based image quality assessment on VMIs

A task-based image quality assessment was performed on VMIs using the iQMetrix-CT software developed by the French Society of Medical Physicists [21]. For each CT system and each energy level, Noise Power Spectrum (NPS), Task-based Transfer Function (TTF) and detectability index were computed based on all the data from the 10 acquisitions. A single calculation for each of these metrics was carried out per energy level.

2.3.1. Noise power spectrum

For each energy level, the NPS was computed in 180 consecutive axial slices (18 slices for each of the 10 acquisitions) by placing four square ROIs (Figure 1B). The sizes of the 4 square ROIs were adjusted according to the phantom's sections: 80 x 80 pixels for 26-cm, 104 x 104 pixels for 31-cm and 120 x 120 pixels for 36-cm diameters.

To quantify changes in noise magnitude, the square root of the area under the NPS1D curve (HU) and the magnitude of the NPS1D peak ($HU^2.mm^2$) were measured. To quantify changes in noise texture, the average spatial frequency (f_{av}, mm^{-1}) of the NPS curve and the spatial frequency of the NPS peak(s) (f_{peak}, mm^{-1}) were measured.

2.3.2. Task-based transfer function

For each VMI, the TTF was computed on iodine inserts at 10 mg/mL (Figure 1C) using the circular edge technique [22]. To minimize the image-noise effect, the TTF was computed from 160 consecutive axial slices (16 slices for each of the 10 acquisitions).

The TTF values at 50% (f_{50}, mm^{-1}) were used to quantify changes in spatial resolution.

2.3.3. Detectability index

A non-prewhitening observer model with an eye filter (d'_{NPWE}) was used to calculate the detectability index (d') for one 10 mm-diameter clinical task approaching the contrast of enhanced

Preprints (www.preprints.org) | NOT PEER-REVIEWED | Posted: 8 August 2023 doi:10.20944/preprints202308.0549.v1

vascular or strongly enhancing parenchymal structures like, for example, a hepatocellular carcinoma [19]. Based on variations in contrast between the phantom's background material and the iodine insert according to energy level, the contrast was set at 1260, 820, 550 and 390 HU for energy levels ranging from 40 to 70 keV.

The shape of the signal was circular and the contrast-profile, Gaussian [23]. Interpretation conditions for calculating d were: a zoom factor of 1.5, a 500-mm viewing distance and the Eckstein visual function [24].

3. Results

The TTF curves obtained for each CT system, each phantom's diameter and each keV are presented in the **Supporting Information**.

3.1. Noise power spectrum

3.1.1. Noise magnitude

For all CT systems and all diameters of phantoms, the noise magnitude decreased as the energy level increased (**Figure 2A**). From 40 to 70 keV, noise magnitude decreased on average for all diameters of phantoms by -59.0% ± 3.3% for SFCT-1st, -57.1% ± 1.6% for SFCT-2nd and -55.4% ± 0.8% for DSCT.

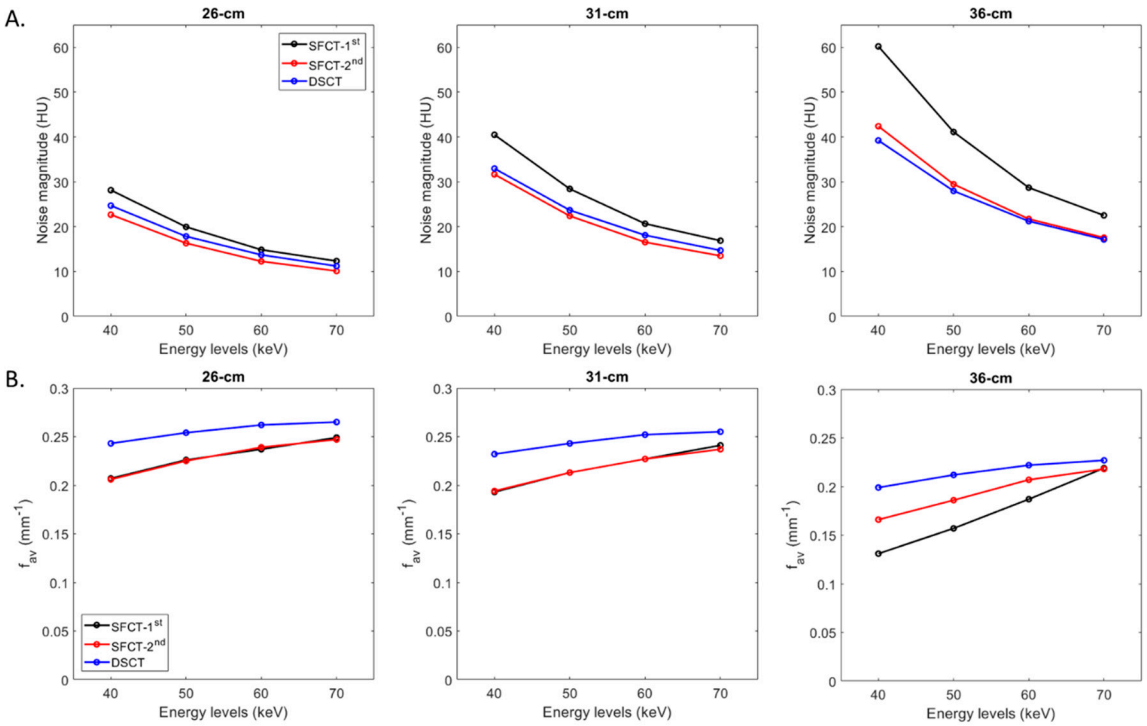

Figure 2. Values of noise magnitude and average Noise Power Spectrum spatial frequencies (f_{av}) obtained for the two generations of split-filter CT platforms (SFCT) and the dual-source CT platform (DSCT) according to phantom diameter and energy level (keV).

For all CT systems and all energy levels, the noise magnitude increased as the phantoms' diameters increased. From diameter 26 cm to 31 cm, the noise magnitude increased on average for all energy levels by 40.5% ± 3.2% for SFTC-1st, 36.3% ± 2.7% for SFCT-2nd and 32.3% ± 1.0% and from 31-cm to 36-cm, 41.4% ± 6.7%, 31.6% ± 1.7% and 17.8% ± 1.0%, respectively.

Whatever the phantom diameter and energy level, the highest noise magnitude values were found with SFCT-1st. For all energy levels, noise magnitude was higher with DSCT than with SFCT-2nd for diameters 26 cm (10.2% ± 1.3%) and 31 cm (7.0% ± 2.5%), and the opposite for diameter 36 cm (-4.2% ± 2.5%).

Preprints (www.preprints.org) | NOT PEER-REVIEWED | Posted: 8 August 2023 doi:10.20944/preprints202308.0549.v1

3.1.2. Noise texture

For all CT systems and all phantom diameters, the average NPS spatial frequencies (f_{av}) increased as the energy level increased (**Figure 2B**). From 40 to 70 keV, f_{av} values increased on average for both SFCTs by 20.1% ± 0.3% for 26 cm and 23.5% ± 1.9% for 31 cm. For the 36 cm-diameter phantom, variations in f_{av} values were more marked for SFCT-1st (from 0.13 to 0.22 mm^{-1}) than for SFCT-2nd (from 0.17 to 0.22 mm^{-1}). For DSCT, f_{av} values increased for all phantom diameters by 11.0% ± 2.7% on average from 40 to 70 keV.

For all CT systems and all energy levels, f_{av} values decreased as the phantoms' diameter increased. From 26 cm to 31 cm in diameter, noise magnitude increased on average for all energy levels by -5.0% ± 1.6% for SFTC-1st, -5.1% ± 0.7% for SFCT-2nd and -4.1% ± 0.4% and from 31 cm to 36 cm, -21.3% ± 10.1%, -11.0% ± 3.1% and -12.5% ± 1.4%, respectively.

Whatever the phantom diameter and energy level, the highest f_{av} values were found with DSCT. For all energy levels, f_{av} values were similar with SFCT-1st and SFCT-2nd for diameters 26 cm and 31cm but for 36 cm, higher f_{av} values were found with SFCT-2nd and all the more so at low keV levels.

With both SFCT systems and all phantom diameters, two NPS peaks were present on the curves for 40, 50 and 60 keV (and 70 keV only for SFCT-1st and 36-cm diameter): one at a spatial frequency of 0.02 to 0.04 mm^{-1} and another at 0.14 to 0.17 mm^{-1} (**Figure 3** and **Table 2**). With DSCT, two NPS peaks were present at 40 keV for all diameters and at all keV only for the 36 cm-diameter phantom. The magnitude of the low frequency NPS peak was higher than the high frequency NPS peak for all systems but the magnitude difference between these two peaks decreased as the energy levels increased.

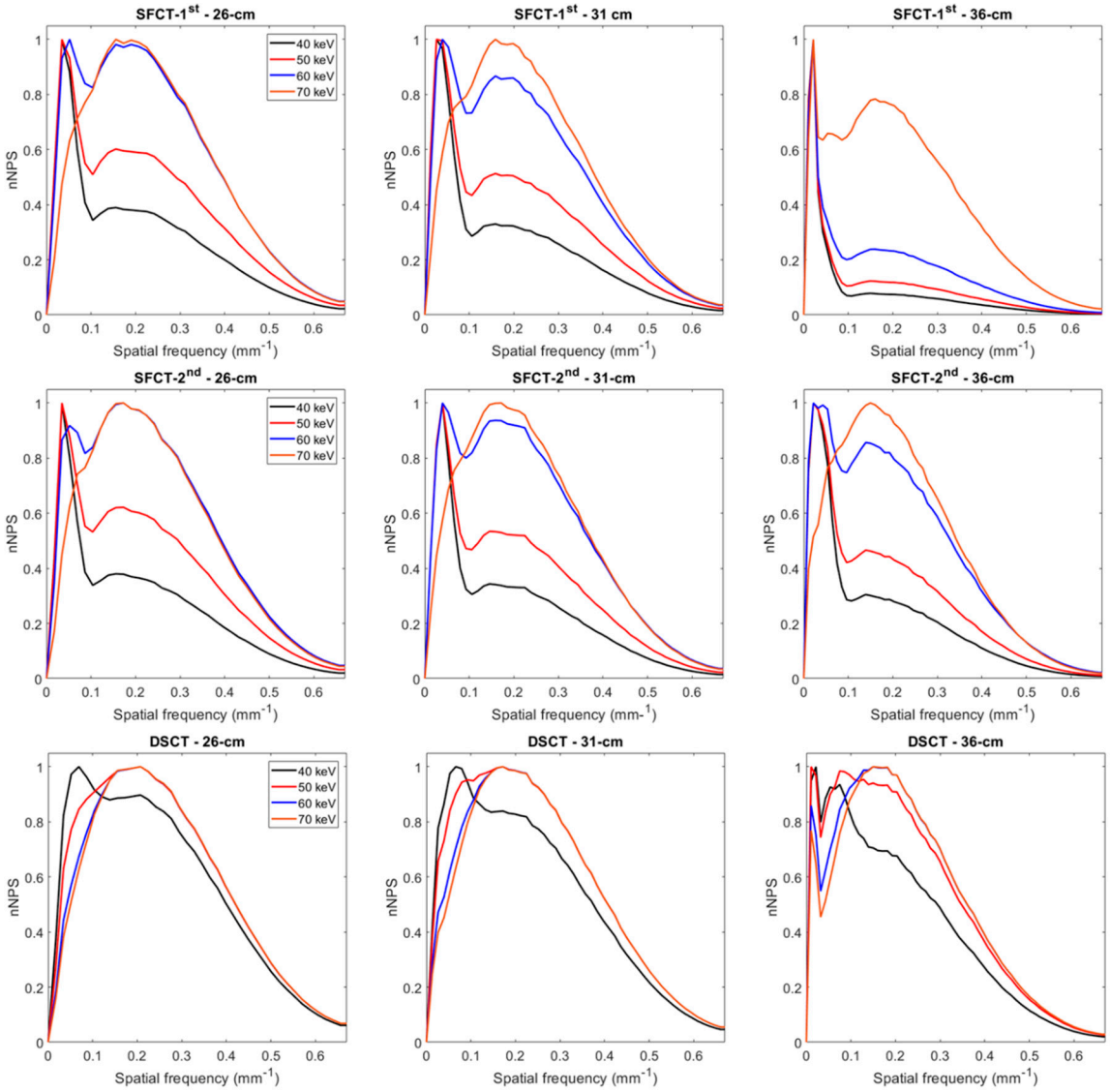

Preprints (www.preprints.org) | NOT PEER-REVIEWED | Posted: 8 August 2023 doi:10.20944/preprints202308.0549.v1

Figure 3. Normalized noise power spectrum (nNPS) curves obtained for the two generations of split filter CT platforms (SFCT) and the dual-source CT platform (DSCT) according to phantom diameter and energy level (keV).

Table 2. Values of noise power spectrum peak(s) and their respective spatial frequencies (f_{peak}) obtained for all energy levels (keV) on the three CT systems.

		NPS peak (HU².mm²)				f_{peak} (mm⁻¹)			
	Diameter	40 keV	50 keV	60 keV	70 keV	40 keV	50 keV	60 keV	70 keV
SFCT-1st	26 cm	3514/1369	1157/696	414/407	288	0.03/0.16	0.03/0.16	0.05/0.16	0.16
	31 cm	8675/2862	2805/1439	933/808	561	0.03/0.16	0.03/0.16	0.05/0.16	0.16
	36 cm	80824/632224	714/30366	606/1574	1350/1057	0.02/0.15	0.02/0.15	0.02/0.16	0.02/0.16
SFCT-2nd	26 cm	2427/922	781/486	261/285	199	0.04/0.16	0.04/0.17	0.05/0.17	0.17
	31 cm	5370/1845	1753/936	566/531	370	0.04/0.15	0.04/0.15	0.04/0.16	0.17
	36 cm	12320/3755	3978/1853	1198/1026	719	0.02/0.14	0.02/0.14	0.02/0.14	0.15
DSCT	26 cm	1131/1015	536	320	214	0.07/0.21	0.21	0.21	0.21
	31 cm	2232/1873	981	579	384	0.07/0.17	0.17	0.17	0.17
	36 cm	4541/4248	1757/1729	826/962	632	0.02/0.07	0.01/0.07	0.01/0.15	0.15

3.2. Task-based transfer function

For all CT systems and all diameters of phantoms, the TTF values at 50% (f_{50}) increased as the energy level increased (**Figure 4** and **Figure A1**). From 40 to 70 keV, f_{50} values increased on average for all diameters of phantoms by 7.6% ± 0.6% for SFTC-1st, 6.3% ± 0.3% for SFCT-2nd and 5.2% ± 0.5% for DSCT.

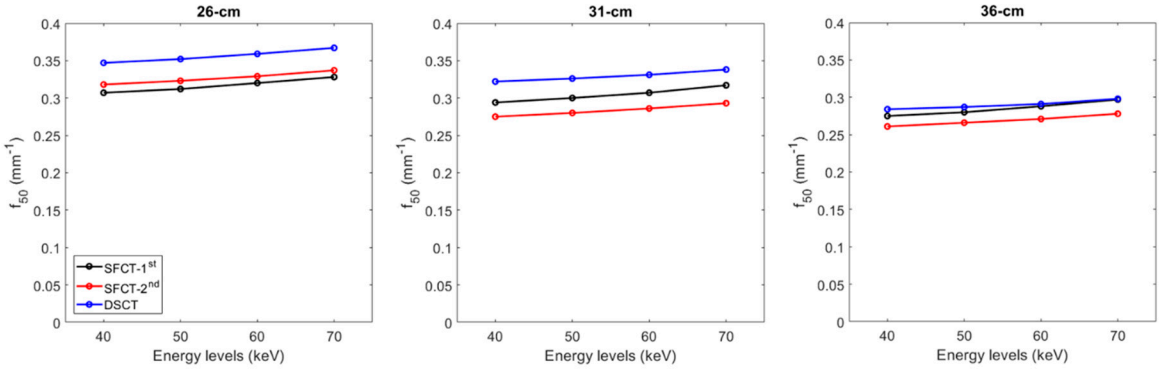

Figure 4. Values of task-based transfer function at 50% (f_{50}) obtained for the two generations of split filter CT platforms (SFCT) and the dual-source CT platform (DSCT) according to phantom diameter and energy level (keV).

For all CT systems and all energy levels, f_{50} values decreased as the diameter phantoms increased. From diameter 26 cm to 31 cm, f_{50} values decreased on average for all energy levels by -3.9% ± 0.4% for SFTC-1st, -13.2% ± 0.2% for SFCT-2nd and -7.6% ± 0.3% and from 31 cm to 36 cm, -6.4% ± 0.2%, -5.1% ± 0.1% and -11.9% ± 0.1%, respectively.

Whatever the phantom diameter and energy level, the highest f_{50} values were found with DSCT, except at 70 keV for the 36 cm-diameter phantom. For all energy levels, f_{50} values were higher with the SFCT-2nd platform than with the SFCT-1st platform for 26 cm-diameter (3.2% ± 0.4%) and the opposite for 31 cm-diameter (-6.9% ± 0.5%) and 36 cm (-5.6% ± 0.7%).

3.3. Detectability indexes

For all CT systems and all phantom diameters, d' values decreased as the energy level increased (**Figure 5**). From 40 to 70 keV, d' values decreased on average for all phantom diameters by -21.7% ± 6.5% for SFTC-1st, -26.0% ± 2.5% for SFCT-2nd and -28.3% ± 0.7% for DSCT.

Preprints (www.preprints.org) | NOT PEER-REVIEWED | Posted: 8 August 2023 doi:10.20944/preprints202308.0549.v1

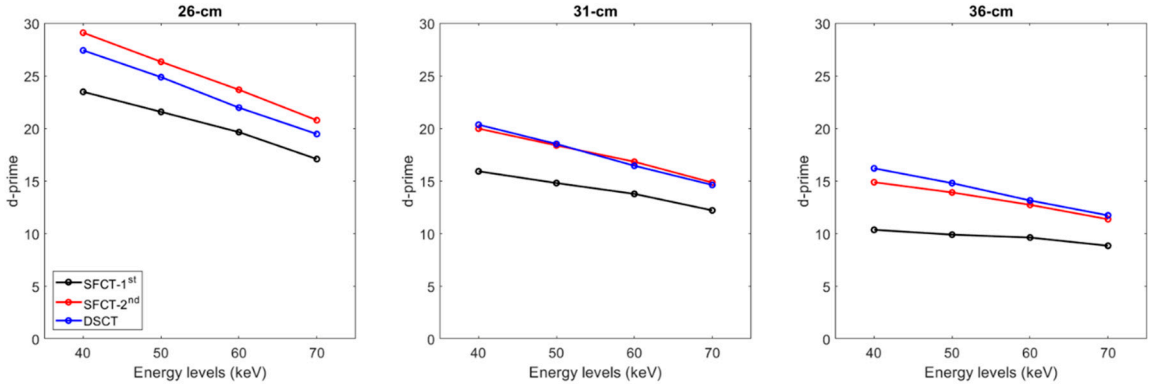

Figure 5. Detectability index (d') values for the simulated lesion obtained for the two generations of split filter CT platforms (SFCT) and the dual-source CT platform (DSCT) according to phantom diameter and energy level (keV).

For all CT systems and all energy levels, d' values decreased as the phantoms' diameter increased. From diameters 26 cm to 31 cm, d' values decreased on average for all energy levels by -30.5% ± 1.6% for SFTC-1st, -29.8% ± 1.3% for SFCT-2nd and -25.3% ± 0.4% and from 31 cm to 36 cm, by -31.5% ± 3.3%, -24.4% ± 0.8% and -20.1% ± 0.2%, respectively.

Whatever the phantom diameter and energy level, the lowest d' values were found with SFCT-1st. For all energy levels, d' values were higher with SFCT-2nd than with DSCT for the 26 cm-diameter phantom (-6.2% ± 0.7%), similar for the 31cm-diameter phantom (-0.3% ± 1.9%) and lower for the 36 cm-diameter phantom (5.4% ± 2.7%).

4. Discussion

In the present study, the performances of three dual-energy CT (DECT) platforms were compared according to the diameter of phantoms. To achieve this goal, a task-based image quality assessment of low-energy-level virtual monoenergetic images was performed. The results showed that, despite increasing the dose level, the greater the phantom's diameter, the greater the image noise and degraded spatial resolution, noise texture and detectability. We also found that lower keV led to an increase in contrast and detectability, despite an increase in noise magnitude and a degradation in noise texture and spatial resolution. Finally, the highest detectability was found with the SFCT-2nd platform for the smallest phantom diameter and, for the dual-source CT platform, with the largest diameter phantom.

The outcomes of the NPS confirmed that the noise magnitude increased as the phantoms' diameter increased [19] and the energy levels decreased [16,17]. For all diameters of phantoms, noise magnitude values were higher with SFCT-1st than with SFCT-2nd and DSCT. The gaps between this platform and the other two decreased as the phantom's diameter decreased. Noise magnitude values were higher with DSCT than with SFCT-2nd for all diameters, except for the 36 cm-diameter phantom. Regarding noise texture, we found that f_{av} values increased as the energy levels increased and as the phantom's diameter decreased. For all diameters of phantoms and for all keVs, the best noise texture was found with DSCT resulting in "fine"noise. Similar noise texture was found with both SFCTs for the 26 cm and 31 cm diameters but the highest f_{av} values were found with the SFCT-2nd for the 36 cm-diameter phantom. These results are consistent with previously published studies on the SFCT-1st which used a different image quality phantom and a different reconstruction kernel (Br40) [16,17] and on DSCT [19]. We also found the presence of two peaks on some NPS curves for all DECT platforms. For all phantom diameters, these two peaks were present on all the NPS curves of both SFCT platforms at 40, 50 and 60 keV. For these two platforms, the magnitude of the NPS peak at low frequencies was higher than the NPS peak's magnitude at high frequencies, the lower the keV and the greater the phantom diameter. This phenomenon was more pronounced with the SFCT-1st than with the SFCT-2nd. With DSCT, these two peaks were present at 40 keV for the three phantom

diameters and at 50 and 60 keV only for the 36 cm-diameter phantom. In addition, the magnitude of the two NPS peaks was similar for both spatial frequencies. The presence of these two NPS peaks had been found in previous studies [16,17] and may be related to distortions in the images or artifacts on the VMIs at the lowest energy levels for these platforms.

The spatial resolution outcomes confirmed that, for the iodine insert at 10 mg/ml, the TTF values at 50% decreased as the phantom's diameter increased [19]. We also confirmed that the f_{50} values decreased as the energy levels decreased [16,17,19]. These results were directly related to noise magnitude and contrast variations according to the phantom's diameter and the energy levels. TTF was calculated using the circular edge technique [22], which generates an Edge Spread Function (ESF) from the difference in HU values between the phantom's background material and the insert. The ESF therefore depends on the noise conditions in the image, as well as on the differences in HU values between the background and the insert. We found that, for the same contrast, image noise increased as the phantom diameter increased, altering the ESF and therefore the resulting TTF. Furthermore, for the same phantom diameter, the reduction in keV resulted, not only in an increase in image noise, but also an increase in contrast. Our results seem to suggest that the impact of noise on the ESF was more marked than that of contrast, since f_{50} values tended to decrease as low keVs decreased. Finally, based on these variations in contrast and image, we found the highest f_{50} values for DSCT, particularly for diameters 26 and 31 cm. With the SFCT platforms, f_{50} values were higher with the SFCT-2nd than with the SFCT-1st for the 26 cm-diameter phantom and the opposite was true for the other diameters.

The results of the detectability index (d') values calculated for the simulated lesions show that d' values peaked at 40 keV and decreased as the energy levels increased. Similar outcomes were obtained by Euler *et al*. for DSCT [19] for the same phantom and by Greffier *et al*. for SFCT-1st and DSCT for another image quality phantom [17]. We also found that the d' values decreased as the phantom's diameter increased. For all diameter phantoms and energy levels, the lowest detectability was found with the SFCT-1st platform. The highest detectability was found with the SFCT-2nd for the 26 cm- diameter phantom and for DSCT for the 36 cm-diameter phantom. Similar d' values were found for DSCT and SFCT-2nd for the 31cm-diameter phantom. As the contrast values were set for each energy level, these outcomes were directly related to the noise magnitude outcomes. Indeed, unlike the TTF, the NPS curves are not normalized and the variations in noise magnitude have a strong impact on the detectability results.

The results of our study show that the spectral performance of the three DECT platforms we studied varied according to the phantoms' diameters and the technology used. Although the dose level increased between the 26 and 36 cm-diameter phantoms, we found that increasing the phantom's diameter altered the detectability, spatial resolution, amplitude and noise texture. Furthermore, different results could be obtained with higher dose levels, particularly for the 36cm-diameter phantom. However, to represent clinical practice as closely as possible, the dose levels were defined from the dose levels of abdomen CT examinations performed on the 3 CT systems used for patients with BMIs similar to those extrapolated for each phantom's diameter. Concerning the technology used, we were able to highlight different results depending on the DECT platform used. Compared to the two other DECT platforms, the SFCT-1st platform, with a limited spectral separation, presented the worst detectability and noise magnitude results and was the most influenced by the increase in phantom diameter. The technological evolutions brought to the SFCT-2nd platform by thickening the Au filter and thinning down the Sn filter for better spectral separation, have led to better results than with the SFCT-1st platform. These improvements have brought the detectability results closer to those obtained with DSCT and even better for the 26 cm-diameter phantom. However, these results must also be interpreted with caution as, in this study, only one pair of kVps (100/Sn150 kVp) out of the 5 available was studied and different results might be obtained with another pair of kVps. In all cases, the results of this study show that the best detectability was obtained at 40 keV for the three CT systems used and therefore suggest that low keV VMIs can be used in clinical routine. In order to guarantee optimal image quality on keV-based VMIs, special

attention must be paid to the dose level used for overweight patients. The results obtained on phantoms in this study must now be confirmed by specific clinical applications on patients.

This study has certain limitations. We performed the acquisitions with only one quantitative reconstruction kernel and only one level of the ADMIRE algorithm was used. Other parameter combinations may provide different outcomes. However, the acquisition and reconstruction parameters used in this study were those used in clinical routine on all DECT systems assessed. Also, we did not use a tube current modulation system on the 3 CT systems. This choice made to guarantee similar dose levels in each phantom diameter for each CT system assessed. Finally, only one task function was chosen to model the detection of contrast-enhanced lesion, with contrast defined according to contrast value variations relative to the VMIs for the one iodine insert available in the Mercury v4.0 phantom. This method was chosen to take into account the variations in contrast of the simulated lesion according to energy level. However, a clinical contrast-enhanced study on lesions of a known specific size should really be carried out now to confirm our results.

5. Conclusions

The outcomes of the present study confirmed that spectral performance depends on the DECT platform and the phantom's diameter. Increasing the phantom's diameter increased the image noise and degraded spatial resolution, noise texture and detectability, despite the increase in dose level. Changing the thickness of tin and gold filters on the SFCT-2nd platform has led to lower noise magnitude and better detectability than with the SFCT-1st. Compared with the DSCT platform, the SFCT-2nd had the lowest noise magnitude and highest detectability for the smallest phantom diameter, and the opposite was true for the largest diameter.

Author Contributions: Conceptualization, J.G. and D.D.; methodology, J.G.; software, J.G.; validation, J.G, C.V.N.T; I.F. and D.D.; formal analysis, J.G, C.V.N.T; I.F. and D.D.; investigation, J.G.; resources, J.P.B.; data curation, J.G, C.V.N.T; I.F. and D.D.; writing—original draft preparation, J.G, C.V.N.T; I.F;, J.F, J.P.B. and D.D.; writing—review and editing, J.G, C.V.N.T; I.F;, J.F, J.P.B. and D.D.; visualization, J.G.; supervision, J/P/B and J.F.; funding acquisition, J.G, C.V.N.T; I.F. and D.D.

Funding: Please add: This research received no external funding.

Institutional Review Board Statement: Not applicable" for studies not involving humans or animals.

Informed Consent Statement: Not applicable.

Data Availability Statement: The data presented in this study are available from the corresponding author upon reasonable request.

Acknowledgments: We wish to thank Teresa Sawyers, medical writer at the B.E.S.P.I.M., Nîmes University Hospital, France, for her help in editing this manuscript. We also thank Cédric Croisille (clinical scientist at Siemens Healthineers) for his help in carrying out this study.

Conflicts of Interest: The authors declare no conflict of interest.

Appendix A

Preprints (www.preprints.org) | NOT PEER-REVIEWED | Posted: 8 August 2023 doi:10.20944/preprints202308.0549.v1

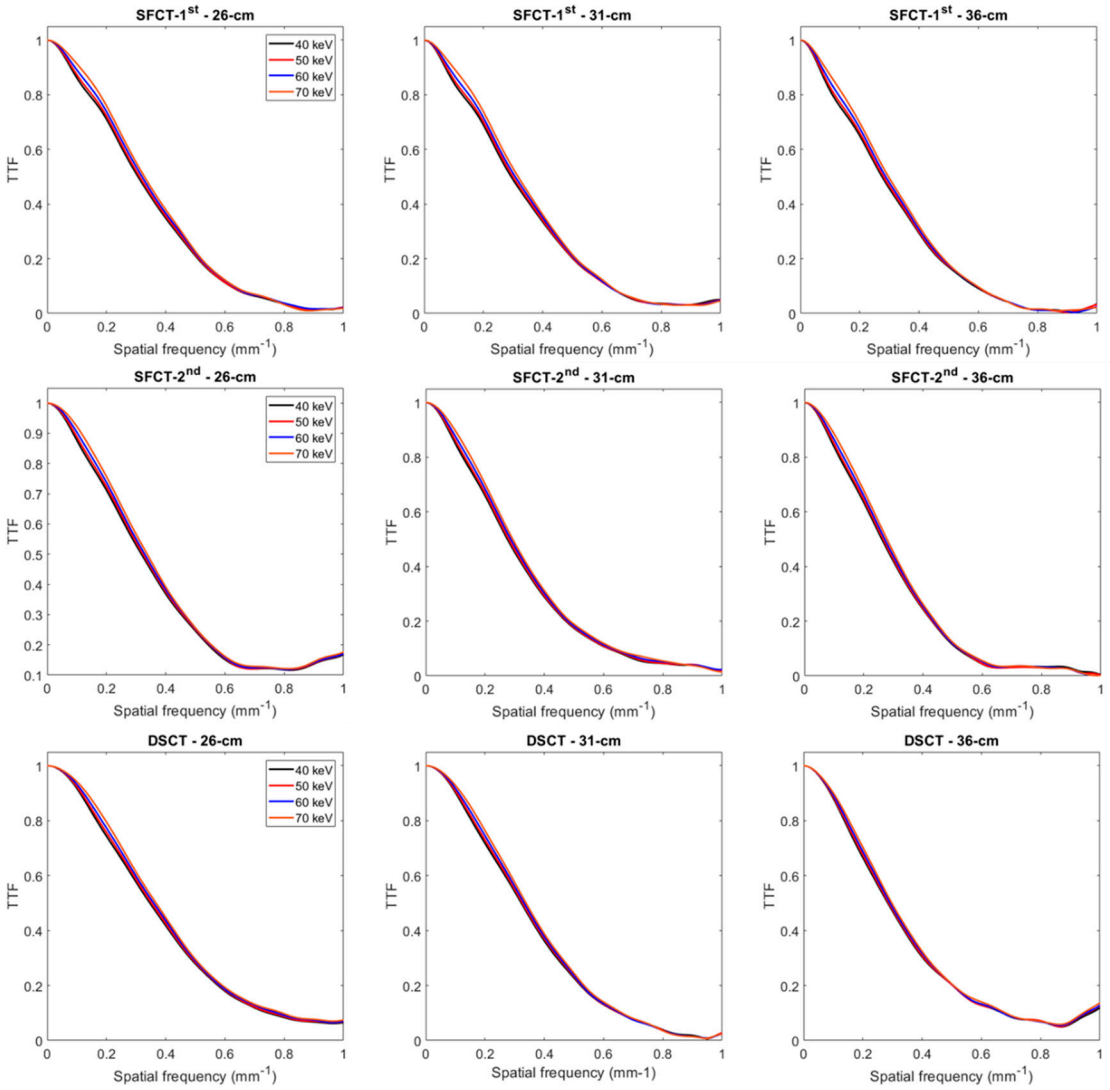

Figure A1. Task-based transfer function (TTF) curves for the iodine insert at 10 mg/ml obtained for the two generations of split filter CT platforms (SFCT) and the dual-source CT platform (DSCT) according to the phantom's diameter and the energy level (keV).

References

1. Greffier, J.; Villani, N.; Defez, D.; Dabli, D.; Si-Mohamed, S. Spectral CT imaging: Technical principles of dual-energy CT and multi-energy photon-counting CT. Diagn Interv Imaging 2023, 104, 167-177, doi:10.1016/j.diii.2022.11.003.
2. McCollough, C.H.; Leng, S.; Yu, L.; Fletcher, J.G. Dual- and Multi-Energy CT: Principles, Technical Approaches, and Clinical Applications. Radiology 2015, 276, 637-653, doi:10.1148/radiol.2015142631.
3. Willemink, M.J.; Noel, P.B. The evolution of image reconstruction for CT-from filtered back projection to artificial intelligence. Eur Radiol 2019, 29, 2185-2195, doi:10.1007/s00330-018-5810-7.
4. Goo, H.W.; Goo, J.M. Dual-Energy CT: New Horizon in Medical Imaging. Korean J Radiol 2017, 18, 555-569, doi:10.3348/kjr.2017.18.4.555.
5. Greffier, J.; Frandon, J.; Durand, Q.; Kammoun, T.; Loisy, M.; Beregi, J.P.; Dabli, D. Contribution of an artificial intelligence deep-learning reconstruction algorithm for dose optimization in lumbar spine CT examination: A phantom study. Diagn Interv Imaging 2023, 104, 76-83, doi:10.1016/j.diii.2022.08.004.
6. Greffier, J.; Frandon, J.; Larbi, A.; Beregi, J.P.; Pereira, F. CT iterative reconstruction algorithms: a task-based image quality assessment. Eur Radiol 2020, 30, 487-500, doi:10.1007/s00330-019-06359-6.
7. Greffier, J.; Hamard, A.; Pereira, F.; Barrau, C.; Pasquier, H.; Beregi, J.P.; Frandon, J. Image quality and dose reduction opportunity of deep learning image reconstruction algorithm for CT: a phantom study. Eur Radiol 2020, 30, 3951-3959, doi:10.1007/s00330-020-06724-w.

8. Jungblut, L.; Abel, F.; Nakhostin, D.; Mergen, V.; Sartoretti, T.; Euler, A.; Frauenfelder, T.; Martini, K. Impact of photon counting detector CT derived virtual monoenergetic images and iodine maps on the diagnosis of pleural empyema. Diagn Interv Imaging 2023, 104, 84-90, doi:10.1016/j.diii.2022.09.006.
9. Boccalini, S.; Dessouky, R.; Rodesch, P.A.; Lacombe, H.; Yagil, Y.; Lahoud, E.; Erhard, K.; Brendel, B.; Coulon, P.; Langlois, J.B., et al. Gadolinium K-edge angiography with a spectral photon counting CT in atherosclerotic rabbits. Diagn Interv Imaging 2023, 10.1016/j.diii.2023.05.002, doi:10.1016/j.diii.2023.05.002.
10. Cosset, B.; Sigovan, M.; Boccalini, S.; Farhat, F.; Douek, P.; Boussel, L.; Si-Mohamed, S.A. Bicolor K-edge spectral photon-counting CT imaging for the diagnosis of thoracic endoleaks: A dynamic phantom study. Diagn Interv Imaging 2023, 104, 235-242, doi:10.1016/j.diii.2022.12.003.
11. Greffier, J.; Frandon, J. Spectral photon-counting CT system: Toward improved image quality performance in conventional and spectral CT imaging. Diagn Interv Imaging 2021, 102, 271-272, doi:10.1016/j.diii.2021.02.003.
12. Marin, D.; Boll, D.T.; Mileto, A.; Nelson, R.C. State of the art: dual-energy CT of the abdomen. Radiology 2014, 271, 327-342, doi:10.1148/radiol.14131480.
13. Chandarana, H.; Megibow, A.J.; Cohen, B.A.; Srinivasan, R.; Kim, D.; Leidecker, C.; Macari, M. Iodine quantification with dual-energy CT: phantom study and preliminary experience with renal masses. AJR Am J Roentgenol 2011, 196, W693-700, doi:10.2214/AJR.10.5541.
14. Agrawal, M.D.; Pinho, D.F.; Kulkarni, N.M.; Hahn, P.F.; Guimaraes, A.R.; Sahani, D.V. Oncologic applications of dual-energy CT in the abdomen. Radiographics 2014, 34, 589-612, doi:10.1148/rg.343135041.
15. Wang, Q.; Shi, G.; Qi, X.; Fan, X.; Wang, L. Quantitative analysis of the dual-energy CT virtual spectral curve for focal liver lesions characterization. Eur J Radiol 2014, 83, 1759-1764, doi:10.1016/j.ejrad.2014.07.009.
16. Greffier, J.; Si-Mohamed, S.; Dabli, D.; de Forges, H.; Hamard, A.; Douek, P.; Beregi, J.P.; Frandon, J. Performance of four dual-energy CT platforms for abdominal imaging: a task-based image quality assessment based on phantom data. Eur Radiol 2021, 31, 5324-5334, doi:10.1007/s00330-020-07671-2.
17. Greffier, J.; Si-Mohamed, S.; Guiu, B.; Frandon, J.; Loisy, M.; de Oliveira, F.; Douek, P.; Beregi, J.P.; Dabli, D. Comparison of virtual monoenergetic imaging between a rapid kilovoltage switching dual-energy computed tomography with deep-learning and four dual-energy CTs with iterative reconstruction. Quant Imaging Med Surg 2022, 12, 1149-1162, doi:10.21037/qims-21-708.
18. Ren, T.; Zhang, W.; Li, S.; Deng, L.; Xue, C.; Li, Z.; Liu, S.; Sun, J.; Zhou, J. Combination of clinical and spectral-CT parameters for predicting lymphovascular and perineural invasion in gastric cancer. Diagn Interv Imaging 2022, 103, 584-593, doi:10.1016/j.diii.2022.07.004.
19. Cester, D.; Eberhard, M.; Alkadhi, H.; Euler, A. Virtual monoenergetic images from dual-energy CT: systematic assessment of task-based image quality performance. Quant Imaging Med Surg 2022, 12, 726-741, doi:10.21037/qims-21-477.
20. Szczykutowicz, T.P.; Michaelson, B.S. USING THE GAMMEX MERCURY 4.0™ PHANTOM FOR COMMON CLINICAL TASKS IN CT. White-Paper Mercury4.0 2018.
21. Greffier, J.; Barbotteau, Y.; Gardavaud, F. iQMetrix-CT: New software for task-based image quality assessment of phantom CT images. Diagn Interv Imaging 2022, 103, 555-562, doi:10.1016/j.diii.2022.05.007.
22. Richard, S.; Husarik, D.B.; Yadava, G.; Murphy, S.N.; Samei, E. Towards task-based assessment of CT performance: system and object MTF across different reconstruction algorithms. Med Phys 2012, 39, 4115-4122, doi:10.1118/1.4725171.
23. Samei, E.; Bakalyar, D.; Boedeker, K.L.; Brady, S.; Fan, J.; Leng, S.; Myers, K.J.; Popescu, L.M.; Ramirez Giraldo, J.C.; Ranallo, F., et al. Performance evaluation of computed tomography systems: Summary of AAPM Task Group 233. Med Phys 2019, 46, e735-e756, doi:10.1002/mp.13763.
24. Eckstein, M.; Bartroff, J.; Abbey, C.; Whiting, J.; Bochud, F. Automated computer evaluation and optimization of image compression of x-ray coronary angiograms for signal known exactly detection tasks. Opt Express 2003, 11, 460-475, doi:10.1364/oe.11.000460.